EDGE ARTICLE

Check for updates

Single-chain magnet behavior in a finite linear hexanuclear molecule†

Felix Houard, [iD] [a] Frederic Gendron, [iD] [a] Yan Suffren, [iD] [a] Thierry Guizouarn,[a] Vincent Dorcet,[a] Guillaume Calvez, [iD] [a] Carole Daiguebonne, [iD] [a] Olivier Guillou, [iD] [a] Boris Le Guennic, [iD] [a] Matteo Mannini [iD] [b] and Kevin Bernot [iD] *[ac]

The careful monitoring of crystallization conditions of a mixture made of a Tb[III] building block and a substituted nitronyl-nitroxide that typically provides infinite coordination polymers (*chains*), affords a remarkably stable linear hexanuclear molecule made of six Tb[III] ions and five NIT radicals. The *hexanuclear units* are double-bridged by water molecules but *ab initio* calculations demonstrate that this bridge is inefficient in mediating any magnetic interaction other than a small dipolar antiferromagnetic coupling. Surprisingly the *hexanuclears*, despite being finite molecules, show a single-chain magnet (SCM) behavior. This results in a magnetic hysteresis at low temperature whose coercive field is almost doubled when compared to the *chains*. We thus demonstrate that finite linear molecules can display SCM magnetic relaxation, which is a strong asset for molecular data storage purposes because 1D magnetic relaxation is more robust than the relaxation mechanisms observed in single-molecule magnets (SMMs) where under-barrier magnetic relaxation can operate.

Introduction

Single-chain magnets (SCMs)[1,2] are molecules whose magnetic relaxation is confined in one dimension. An efficient SCM combines a strong interaction between its anisotropic spin carriers with a good magnetic insulation from the neighboring chains.[3–5] At low temperature, such topologic and magnetic configurations give rise to a correlation length between spin carriers that can be considered as a 1D magnetic domain on which magnetic information can be encrypted.[6]

The design of new SCMs with enhanced magnetic behavior[7–16] relies on the use of coordination chemistry tools and can be performed in two ways. First, the selection of metal centers and their surrounding ligands permits an optimization of the magnetic behavior of the SCMs by enhancing the magnetic anisotropy of the metal ion and/or the ratio between intra- and interchain magnetic interactions.[17–19] Second, a careful tuning of the organic ligands can provide new properties to the magnetic chains such as luminescence,[20–22] photomagnetic behavior,[23–25]

[a]Univ Rennes, INSA Rennes, CNRS, ISCR (Institut des Sciences Chimiques de Rennes), UMR 6226, F 35000, Rennes, France. E-mail: kevin.bernot@insa-rennes.fr

[b]LAboratory for Molecular Magnetism (LA.M.M.), Dipartimento di Chimica "Ugo Schiff"(DICUS), Università degli Studi di Firenze, INSTM, UdR Firenze, Via della Lastruccia n. 3, Sesto Fiorentino (FI), 50019, Italy

[c]Institut Universitaire de France, 1 rue Descartes, 75005, Paris, France

magnetic switching,[14,26–29] magneto-electric coupling,[30,31] magneto-chiral dichroism,[32] spin helicity,[33] or gelation ability.[34,35] We have explored this second strategy recently using Tb[III] ions and nitronyl-nitroxide radicals[36–48] substituted by alkyl chains. We showed that the chains of formula $[(Tb(hfac)_3)_6(-NITPhOHexyl)_5(H_2O)_2]_n$ (with hfac$^-$ = hexafluoroacetylacetonate and NIT-Ph-*O*-Hexyl = 2-(4′-(hexyloxy)phenyl)-4,4,5,5-tetramethylimidazolin-1-oxyl-3-oxide) can be organized in the crystal packing to form chiral supramolecular nanotubes of single-chain magnets.[49] In this paper, we report how *chains* can be converted into finite hexanuclear species (latter called *hexanuclears*) with an enhanced SCM behavior.

Results and discussion

Hexanuclear formation process

The compound is obtained by the reaction of equimolar amounts of NIT-Ph-*O*-Hexyl with $Tb(hfac)_3 \cdot 2H_2O$ in boiling heptane (see ESI† for details). The reaction mixture crystalizes after three days at ambient temperature.

Usually very thin needle-like light green crystals of *chains* appear but in some rare cases we noticed that plate-like crystals polymorph could be observed during crystal growth (Fig. 1 and S1†). Needle and plates have chemical similarities since they share the same vibrational bands and became quickly amorphous when removed from the mother solution (see Fourier Transform Infra-Red spectroscopy (FTIR) and Powder X-ray Diffraction (PXRD), Fig. S2 and S3†). After a careful screening of the crystallization conditions, we observed that
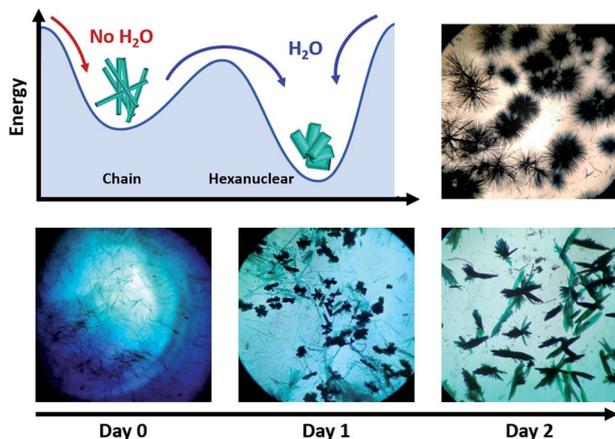
Fig. 1 (top left) Possible crystallization mechanism of the *hexanuclears*; (top right) picture of crystals of *chains* obtained in dry atmosphere; (bottom) observation of the progressive changes observed in the crystallization batch where needles (*chains*) disappears and plates are formed (*hexanuclears*) under water-saturated conditions (×10 magnification).

moisture triggers the predominance of plates over needles: crystals of *chains* always appear first and can be converted into plates in 3 days of slow evaporation if humidity level is high enough (Fig. 1). Based on this observation we have been able to obtain pure batches of plate-like crystals, by conducting crystallization in water-saturated condition in closed vials (see ESI†). Accordingly, what was an awkward by-product in the synthesis of *chains*, could be rationally investigated.

Crystal structure of the hexanuclears

Crystal structure determination on plate-like crystals suggests the formation of Tb^{III} *hexanuclears* of formula $[(Tb(hfac)_3)_6(NITPhOHexyl)_5(H_2O)_2] \cdot CHCl_3 \cdot C_7H_{16}$. They crystallize in a monoclinic system, space group $P2_1/n$ (Tables S1 and S2,† Fig. 2, S3 and S4†). The asymmetric unit is made of five NIT radicals that alternate with six $Tb(hfac)_3$ units to form a linear molecule ended by water capped $Tb(hfac)_3$ units.

All Tb^{III} ions are eight coordinated by eight oxygen atoms (six from the $hfac^-$ ligands and two from NIT radicals) excepted terminal Tb1 and Tb6 ions where one radical is substituted by a water molecule. Coordination polyhedra are D_{2d} triangular dodecahedra for Tb1, Tb2, Tb3, Tb4 and Tb5 (the first two are also close to D_{4d} square antiprism) and D_{4d} square antiprism for Tb6 (Table S3†). $Tb-O_{rad}$ distances are in the range of 2.36–2.41 Å and shortest intramolecular distance between Tb^{III} ions within the molecule is 8.40 Å. These values are close to the ones reported on *chains* and highlight the chemical similarities between the two derivatives.

Molecules based on β-diketonate and NIT units usually host numerous π-stacking interaction pathways.[50] This is again observed here and inter-centroid distances in the *hexanuclears* are similar to the one observed in *chains* ($d_{\pi-\pi} = 3.4$–3.9 Å) but with more tilted orientations ($\alpha = 9.6$–24.3°, except for Tb4–Tb5 rings where $\alpha = 3.7$–4.2°) indicating potentially weaker π-interactions.
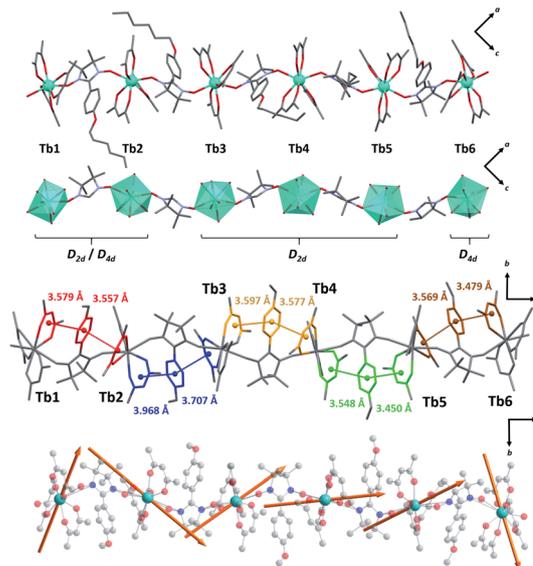

Fig. 2 (From top to bottom with solvent molecules, hydrogen and fluorine atoms omitted) Representations of the asymmetric unit; simplified magnetic backbone that highlight the coordination polyhedra; representation of the stacking interactions; representation of the easy axes of the magnetization for the Tb^{III} ground state on the model compound of the *hexanuclear* (see ESI†).

The terminal water molecules of two consecutive *hexanuclears* interact two-by-two in a very similar way as the one observed in the crystalline $Tb(hfac)_3$ dihydrate.[51,52] This interaction is tailored by the strong Lewis acidity of the $Tb(hfac)_3$ units that favour interaction between the electron-poor water oxygen atoms of two neighboring molecules. This induces an intermolecular Tb–Tb distance of 6.05 Å that is shorter than the mean value of the intramolecular one (8.40 Å). This will be a key point for the investigation of the magnetic properties of the *hexanuclears*.

Overall, this non-covalent bonding between consecutive units, coupled with the symmetry operations of the $P2_1/n$ space
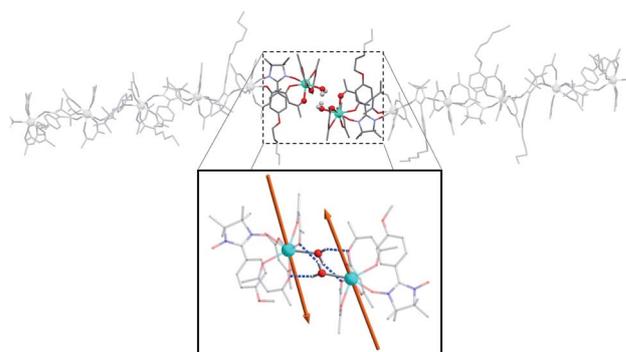

Fig. 3 Representation of two neighbouring *hexanuclears* that stand along the [502] direction, together with the H-bond network between the terminal water molecules highlighted. Tb–Tb distance is 6.05 Å and O···H distance is 2.22 and 2.33 Å (fluorine and hydrogen atoms omitted for clarity). (Inset) Representation of the easy axes of the magnetization for the Tb^{III} ground state in the dimer model that simulates the extremities of the *hexanuclears* (see ESI†).
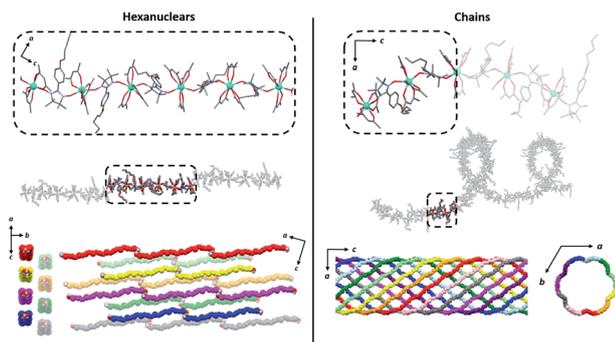
Fig. 4 Comparison of the *hexanuclears* and the *chains*[49] (from top to bottom with solvent molecules, hydrogen and fluorine atoms omitted): representations of the molecules with the asymmetric unit as dotted square; representation of the crystal packing along and perpendicular to the propagation direction of the molecules ([502] direction for the *hexanuclears*, -axis for the *chains*).

group generates a supramolecular arrangement of *hexanuclears* along the [502] direction (Fig. 3 and 4). Perpendicularly to this direction, shortest Tb–Tb interchain distance is 11.33 Å. This excludes any intermolecular magnetic interactions between the molecules as well as long-range magnetic ordering. Finally, one chloroform and one heptane molecules per asymmetric unit are found (Fig. S4†).

It is worth comparing the finite *hexanuclear* molecules obtained here with the previously reported *chains*.[49] At a first glance, one could think that the chains form first and that water molecules cut it in special points to form the finite molecule. However, no obvious "cutting point" can be found on the *chains* using either the symmetry operation of the space group, the number of repeating asymmetric unit, the Tb coordination polyhedron or the calculated easy-magnetic axes orientation (Fig. 4).

One can also compare the two crystallization routes (Fig. 1): (i) the transformation of *chains* into *hexanuclear* units is not strictly a single-crystal-to-single-crystal transformation because it occurs in the mother solution. So, it is likely that the chains decompose and then the presence of water triggers the crystallization of the hexanuclear compounds; (ii) hexanuclear can be obtained directly from the mother solution if the crystallization is conducted in water-saturated conditions. The *chain* crystals (needles) are not observed but directly the *hexanuclear* units (platelets).

The crystal packing is also very different (Fig. 4). *Hexanuclears* are water bridged along the [502] direction and then further stack one over the other. This contrasts with what seen on *chains* where supramolecular interaction between chains induce a helicity and constrain them to be wrapped eleven by eleven to form supramolecular nanotubes that further stack in a hexagonal lattice.

It can be noted that, as far we tested it, variation of the stoichiometry, the temperature or humidity conditions does not allow controlling the nuclearity of the molecule because as soon as humidity is present during the crystallization, *hexanuclears* are obtained. This suggests that this species is particularly stable on the thermodynamic point of view. This is rather surprising because linear polynuclear molecules usually tend to form wheels to gain in stability[53] even when combined in larger edifices.[54]

Stability of the hexanuclears: thermal and luminescent characterization

The *hexanuclears* single-crystals quickly became amorphous when taken off the mother solution. This is due to solvent loss as 10% of the cell volume ($V_{void} = 2577$ Å^3 for a 1.2 Å kinetic radius) is filled with *n*-heptane and chloroform molecules that quickly evaporate. Despite losing their long-range order and diffracting power, crystals are still robust and can be collected easily. Indeed, SEM images show that crystals are still observable under vacuum conditions (Fig. S1†) and don't collapse into a powder. This is probably because the main intermolecular contacts between the hexanuclear units are *via* their alkyl chains, not with the crystallization solvent molecules.

However, to check that a reliable magnetic measurement can be performed on these amorphous compounds, coupled FTIR spectroscopy and thermogravimetric and thermodifferential analyses (TGA/TDA) have been performed on freshly dried amorphous crystals (Fig. S5 and S6†). They show that the compound is stable up to 124 °C (coordinated water molecules departure) and that no other significant gas emission is observed below 200 °C. This sustains the hypothesis that the fast amorphization is due to crystallization solvent loss (chloroform and heptane) and that the molecular skeleton of the compound is preserved at room temperature (no gas emission before full decomposition of the compound at high temperature).

The chemical integrity of the compound can be confirmed using luminescence measurements. Such measurements provide a very sensitive estimation of the stability of NIT-Tb^{III} based compounds[49] because both uncoordinated reactants emit in the visible: a line-shaped green emission for the uncoordinated Tb(hfac)$_3$ unit (because of the efficient antenna effect of the β-diketonate ligand)[55] and a broad red emission for the NIT radical.[56,57] When the two molecules are coordinated, Tb^{III} emission is quenched while the NIT radical emission is blue-shifted by metal–ligand charge transfer (MLCT).[57,58] This is what we observed here with no emission of the free Tb^{III} ion and a blue-shifted NIT radical emission (Fig. 5), indicating the efficient Tb-NIT coordination and the absence of uncoordinated Tb^{III} and NIT radical. Moreover, the optical signature of the *hexanuclears* is different from the ones of the *chains* (Fig. S7†).

All these thermal and luminescent investigations unambiguously demonstrate that the *hexanuclears* are preserved upon crystal amorphization and that magnetic investigation can be trustily performed.

Static (dc) magnetic properties

The temperature dependence of the magnetic susceptibility χ_M has been measured on polycrystalline sample under static field ($H_{DC} = 1000$ Oe). It shows a $\chi_M T_{(300K)}$ value of 72.02 emu K mol^{-1}, close to the theoretical value $\chi_M T_{(300K)} = 72.795$ emu K mol^{-1}
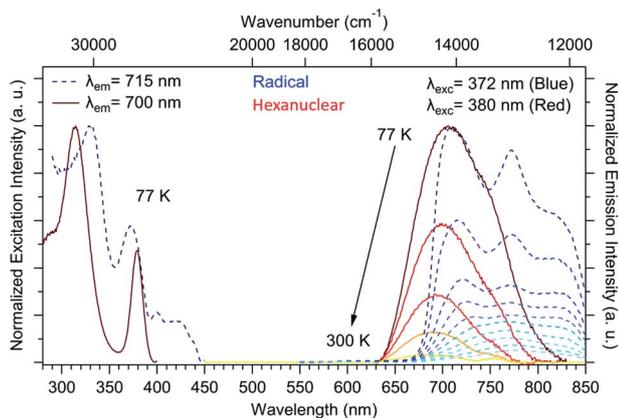
Fig. 5 Solid–state excitation spectra at 77 K ($\lambda_{em} = 715$ and 700 nm) and emission spectra between 77 and 300 K ($\lambda_{ex} = 372$ and 380 nm) for the uncoordinated radical (dark to light blue dotted curves) and the *hexanuclears* (brown to yellow full line curves).

expected for 6 Tb^{III} ions and 5 uncoupled NIT radicals (with $g_S = 2$, $S = \frac{1}{2}$, $g_J = 3/2$ and $J = 6$). By decreasing the temperature, this value slightly increases until 50 K then sharply reaches a maximum of $\chi_M T_{(dc)} = 199.65$ emu K mol^{-1} at 3.5 K. This increase is followed by an abrupt drop due to saturation effects. Hence, a more reliable maximum of $\chi_M T_{(ac)} = 289.54$ emu K mol^{-1} is observed at 2 K for $\nu = 0.019$ Hz ($H_{AC} = 3$ Oe oscillating field). The saturation is also confirmed by the magnetization curve recorded at 2 K that rises very quickly as the field is applied to reach a value of 29.4 μ_B at 50 kOe (Fig. S8†), slightly lower than the theoretical saturation value expected on a polycrystalline sample ($M_s = 32.0$ μ_B). A last confirmation arises from specific heat measurement that does not show any divergence of the specific heat capacity (C_p) in the low temperature region as it can be observed in the presence of long-range magnetic ordering (Fig. S9†).

Theoretical description of the hexanuclears and magnetic coupling

The magnetic anisotropy of each of the Tb^{III} centers can be determined by considering either [Tb(hfac)$_3$(NIT)$_2$] units for the central Tb^{III} ions (Tb2, Tb3, Tb4, Tb5) or [Tb(hfac)$_3$(NIT) (H$_2$O)] units for the terminal Tb^{III} ions (Tb1, Tb6) (see ESI for computational details and models Fig. S10†).

The calculated relative energies of the states deriving from the $^7F_6$ level of the Tb^{3+} ion in the model compounds, and the associated EPR g-factors (for the states exhibiting a pseudo-spin $S = \frac{1}{2}$) are given in Table S4.† In all model compounds, the ground state (GS) corresponds to a non-Kramers doublet that derives formally from the M$_J$ states ± 6 of the $^7F_6$ level. More precisely, the nature of these states results from an admixture by the crystal-field of the different M$_J$ states. The calculated contributions for the GS wave-function are given in Table S5.† The M$_J = \pm 6$ state is the dominant contribution, but a sizable one is calculated from the M$_J = \pm 4$ state. Interestingly, the contribution of the M$_J = \pm 6$ state into the GS wave-function differs significantly between the six model compounds, in

agreement with the small differences observed in the first coordination sphere of the Tb^{III} ions (Table S3†).

The [Tb(1)-NIT$_2$]$^{2-}$ model compound has the lowest M$_J = \pm 6$ contribution (76%), leading to the smallest value for the parallel component of the EPR g-factors ($g_\parallel = 16.58$). By comparison, the [Tb(5)-NIT-H$_2$O]$^-$ model compound exhibits a GS with a EPR g-factor of 17.26 because of the largest contribution (91%) of M$_J = \pm 6$ into the wave-function. This is linked with a trend in the modification of the energetic splitting. In [Tb(2)-NIT$_2$]$^{2-}$, a relatively small energy gap of 16 cm^{-1} is calculated between the GS and ES1, whereas this energy gap increases to 85 cm^{-1} for [Tb(5)-NIT-H$_2$O]$^-$. The overall splitting of the $^7F_6$ level also differs between the six building blocks of the *hexanuclears*, with calculated splitting of 361 and 388 cm^{-1} for [Tb(5)-NIT-H$_2$O]$^-$ and [Tb(6)-NIT-H$_2$O]$^-$, respectively, whereas splitting of 431, 470, 486 and 527 cm^{-1}, are calculated for Tb(1), Tb(2), Tb(4), and Tb(3), respectively.

The orientation of the easy axes of the magnetization for the GS of the six model compounds is shown in Fig. 2 and reveals different orientations. The GS of the model compounds exhibits large magnetic anisotropy, characterized by extremely large parallel components of the EPR g-factors (*c.a.* 17) and perpendicular components equal to zero. For comparison, a pure M$_J = \pm 6$ state would possess a parallel component of 18.0.

For the central Tb centers (Tb2, Tb3, Tb4, Tb5), the easy axis goes mostly along the NIT-Tb-NIT direction as observed on the *chains*. A very different scenario is observed for the terminal Tb1 and Tb6 atoms. As already observed by some of us on mononuclear molecules[59] Tb1 and Tb6 magnetic axes are perpendicular to the Tb-O(water) direction and the plane of the water molecule. The coordinated water is the driving force for the localization of the easy-magnetic axes.

The calculated magnetic susceptibilities and magnetization for the six model compounds are shown in Fig. S11.† At room temperature, very similar $\chi_M T$ values of *ca.* 11.6 cm^3 K mol^{-1} are calculated for all complexes. Due to a non-magnetic ES1 in [Tb(6)-NIT-H$_2$O]$^-$, the decrease in magnitude of $\chi_M T$ is stronger at very low temperature than in the other compounds. On the other hand, the presence of a very low-lying ES1 in [Tb(1)-NIT$_2$]$^{2-}$ and [Tb(2)-NIT$_2$]$^{2-}$ leads to calculated magnetizations at 2 K that do not reach saturation at 5 Tesla, whereas for the other model compounds, the calculated magnetizations saturate at 4.5 μ_B.

On 3d-based chains, straightforward *ab initio* calculations of intrachain coupling constants have been recently reported[60] but are unlikely to be directly applicable on the *hexanuclears.* Indeed, the reliable determination of magnetic interactions on Ln-NIT compounds would require the use of state-of-the-art wave function-based calculations (CASSCF/DDCI) that are challenging even on isolated NIT-Y^{III}-NIT molecules.[61] Moreover, the modelization of the magnetic interaction pathways is trickier here because SCM made of NIT radicals and lanthanide ions are known to host nearest (NIT-Ln) and next-nearest (Ln–Ln, and NIT–NIT) neighbor magnetic interactions, the latter being stronger than the former.[46] Last, the very large asymmetric unit of the *hexanuclears* (6 Tb^{III} ions and five radicals) complicate further the study and does not allow for a reliable
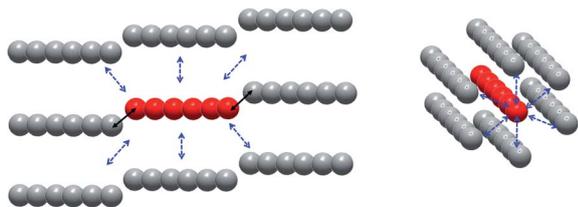
Scheme 1 Representation of the intermolecular magnetic interactions between a given *hexanuclear* (red) and its neighbors (grey) parallel or perpendicular to the [502] direction (interaction mediated *via* the water bridge as full black arrows and through-space interactions as dotted blue arrows).
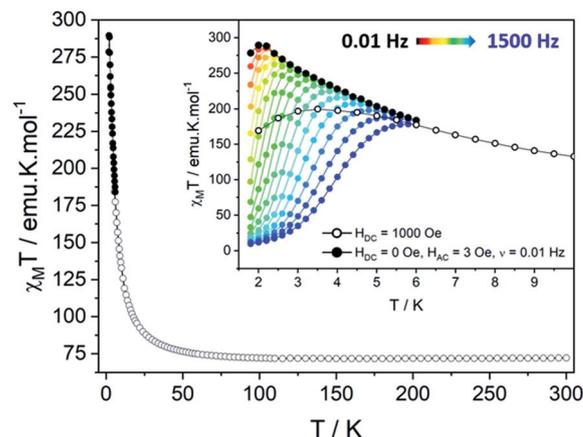

Fig. 6 (Top) Temperature dependence of $\chi_M T$ for the *hexanuclears* measured with $H_{dc} = 1000$ Oe (black circles) and reconstructed from ac measurements with $H_{dc} = 0$ Oe, $H_{ac} = 3$ Oe, $\nu = 0.01$ Hz (black dots). In inset, a zoom in the low temperature region with the ac data for frequencies from $\nu = 0.01$ Hz (black) to 1500 Hz (blue).

determination of all of the intramolecular magnetic interactions.

On the intermolecular point of view two main interaction pathways can be considered (Scheme 1): perpendicular (dotted arrows) or along the [502] direction (full arrows). For the first case, the Tb–Tb distance is >11 Å so significant magnetic interaction can be discarded. For the second one, Tb–Tb distance is 6.05 Å and hexanuclear units are water bridged by the terminal water molecules (Fig. 3). Even if specific heat measurements demonstrate that no 3D magnetic ordering is observed, it is crucial to determine the nature and value of a potential interaction to assess if the compound behaves as an alternating chain of coupled hexanuclear units or if *hexanuclears* are more or less magnetically isolated.

We used the dimer model (Fig. S10†) to calculate the magnetic susceptibility as a function of the temperature (Fig. S12†). At low temperature, the decrease of the $\chi_M T$ product is reinforced by a small intramolecular antiferromagnetic (AFM) interaction between the two Tb^{3+} ions. Magnetic exchange is neglected because of the large Tb–Tb distance and the isotropic dipolar contribution of the AFM interaction is found of *ca.* -0.11 cm^{-1}. This value can be readily understood by the almost collinear orientation of the easy magnetic axes as shown on Fig. 3.

Supramolecular interactions are efficient to build SCMs based on 3d metal ions[62,63] whereas they are not with 4f ions because of the inner character of their orbitals. Accordingly, the very small dipolar coupling observed between Tb1 and Tb6 ions is unlikely to be strong enough to propagate a correlation length beyond the *hexanuclears* because it is several orders of magnitude smaller than the ones operating in the molecule as demonstrated on similar NIT-based compound.[37,46–48,61] Accordingly, the divergence of the $\chi_M T$ at low temperature (Fig. 6) can be ascribed to the creation of a correlation length that is confined within each *hexanuclear*.

When the temperature is lowered the $\chi_M T$ product varies as $\chi_M T = C_{eff} \exp(\Delta_\xi / k_B T)$ where C_{eff} is the effective Curie constant, k_B the Boltzmann constant and Δ_ξ the correlation energy required to create a domain wall that can be extracted from dc or ac measurements ($\Delta_{\xi(dc)}$ or $\Delta_{\xi(ac)}$, respectively). These values were estimated at $C_{eff} = 66.86$ emu K mol^{-1} and $\Delta_{\xi(dc)} = 6.9 \pm 0.1$ K ($R^2 = 0.99842$) (Fig. S12†). The $\Delta_{\xi(dc)}$ value is comparable to the one observed on the *chains* derivative ($\Delta_{\xi(dc)} = 5.5 \pm 0.5$ K)

(Table 1). We performed diamagnetic doping of the *hexanuclears* by Y^{III} or Lu^{III} ions to evaluate statistically the dimension of the correlation length. SEM/EDS measurements showed expected Tb/Y or Tb/Lu ratio when pointing at large areas. But as soon as local measurements were taken in spot mode very strong discrepancies occur as a sign of segregation between hexanuclear units made of Tb and others of Y/Lu ions. Consequently, this approach has been dismissed.

Dynamic (ac) magnetic properties

Clear out-of-phase susceptibility (χ_M'') signal is observed in absence of dc field at 2 K (Fig. 7, S14–S15†). The magnetic relaxation accelerates when H_{dc} is increased as expected for an SCM (Fig. S16†).[64,65] This is the opposite in-field behavior as the one observed on ferromagnetically-coupled SMM[24] that would present an increase of $\chi_M T$ at low temperature but an enhanced in-field dynamic magnetic behavior.

The out-of-phase susceptibility χ_M'' shows frequency dependence up to 6 K, characteristic of slow relaxation of the magnetization[66] with no broadening as one would observed if the six crystallographically independent Tb^{III} ions were not correlated enough and relaxed independently.

The corresponding relaxation times τ were extracted using a generalized Debye model[67,68] and fitted according to an Arrhenius law $\tau = \tau_0 \exp(\Delta_{eff} / k_B T)$ where Δ_{eff} is the effective energy barrier (Table S6†).[69]

The relaxation dynamics of SCMs is ruled by two thermally activated processes that correspond to the finite- and infinite-magnetic chains when compared to the correlation length.[70,71] Their effective energy barriers can be expressed respectively as $\Delta_F = \Delta_A + \Delta_{\xi(ac)}$, and $\Delta_I = \Delta_A + 2\Delta_{\xi(ac)}$ (with Δ_A the anisotropic contribution of the Tb^{III} ion and $\Delta_{\xi(ac)}$ the correlation length extracted from dynamic magnetic measurements). In our case, the finite-regime is characterized by $\Delta_F / k_B = 24.4 \pm 0.5$ K with $\tau_F = (1.1 \pm 0.2) \times 10^{-6}$ s ($R^2 = 0.99884$), while for the infinite-regime, $\Delta_I / k_B = 27.7 \pm 0.1$ K with $\tau_I = (2.7 \pm 0.1) \times 10^{-7}$ s

Table 1 Summary of the main magnetic values for *chains*[49] and *hexanuclears*

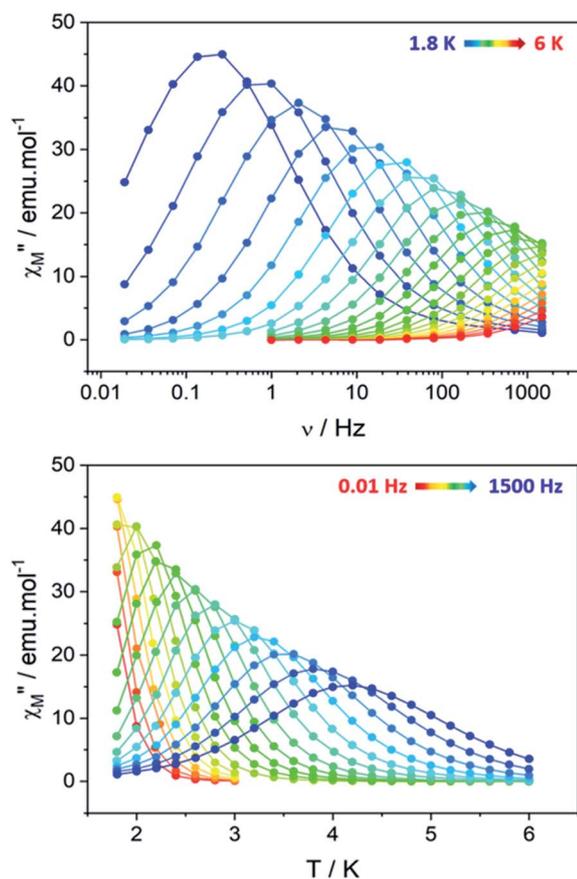|	Chains	Hexanuclears
$\Delta_{\xi(\mathrm{dc})}$ (K)	5.5 ± 0.5	6.9 ± 0.1
$\Delta_\mathrm{I}/k_\mathrm{B}$ (K)/τ_I (s)	$29.6 \pm 0.5/3.4 \pm 0.5 \times 10^{-8}$	$27.7 \pm 0.1/2.7 \pm 0.1 \times 10^{-7}$
$\Delta_\mathrm{F}/k_\mathrm{B}$ (K)/τ_F (s)	$25.5 \pm 0.2/2.4 \pm 0.3 \times 10^{-7}$	$24.4 \pm 0.5/1.1 \pm 0.2 \times 10^{-6}$
$\Delta_{\xi(\mathrm{ac})}$ (K)	4.1 ± 0.7	3.3 ± 0.6
T^* (K)	2.1	2.4
n (dc and ac)	17; 5	18; 3
α (at 1.8 K)	0.615	0.374
H_c (Oe)	2400	4100
M_R (μ_B/%M_sat)	2.09/38%	19.83/62%
T_B (K)	1.39 ± 0.02	1.34 ± 0.03

Fig. 7 ac magnetic measurements measured on the *hexanuclears* ($H_\mathrm{dc} = 0$ Oe, $H_\mathrm{ac} = 3$ Oe): (top) frequency dependence of the out-of-phase (χ_M'') susceptibility; (bottom) temperature dependence of the out-of-phase susceptibility.

An extended Debye model[16] is applied to determine the distribution (α) of the relaxation times (Table S7†). As a reminder, the α value for an ideal relaxation dynamic tends
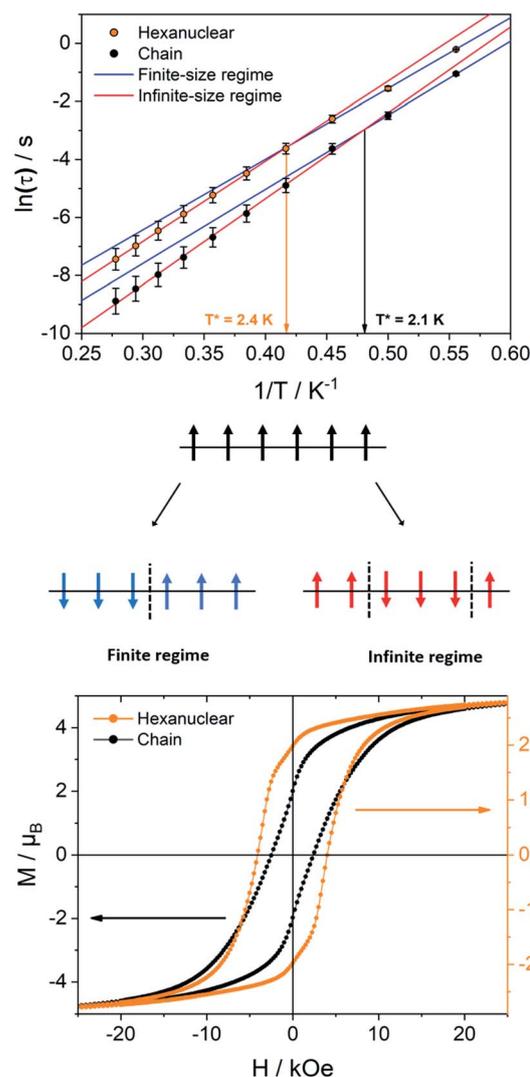

Fig. 8 (Top) Arrhenius plots of *hexanuclears* (circles) and *chains* (dots) with fitting of the finite (blue) and infinite-size (red) regimes; (middle) scheme of the relaxation regimes for a 3 spin correlation; (bottom) hysteresis at 0.5 K measured with a field sweep rate of 15 Oe s^{-1} for the *hexanuclears* (orange) and *chains* (black).

($R^2 = 0.99989$), with a crossover temperature between the two regimes at $T^* = 2.4$ K (Fig. 8). Hence, the correlation energy Δ_ξ can be estimated as $\Delta_{\xi(\mathrm{ac})} = \Delta_\mathrm{I} - \Delta_\mathrm{F} = 3.3 \pm 0.6$ K. This value is rather small but is in line with what found on the *chains* derivative. Δ_ξ can be linked to the average number n of the correlated magnetic anisotropic units through $n \approx 2\xi \approx \exp(\Delta_\xi/k_\mathrm{B}T^*)$. Using $\Delta_{\xi(\mathrm{ac})}$ and given the small values and the large confidence interval, n is comprised between 3 and 5. This is in agreement with the observation of both finite and infinite regimes in this hexanuclear molecule ($n = 6$).

towards zero (all the molecules share the same single relaxation time τ) while it is 1 for a totally disordered relaxation scheme. In our case, α spread from 0.16 at 4 K to 0.37 at 1.8 K (Fig. S17†) and only one semi-circle is observed ruling out the possibility of an SMM behavior as several relaxations should be observed because the six Tb^{III} ions show different crystal-field splitting and different M_J contributions to the ground-state wave-function. Additionally, 97% of the sample relaxes slowly at 1.8 K $(1 - (\chi_s/\chi_T) = 97\%$ with χ_s and χ_T the adiabatic and the isothermal susceptibility, respectively).

The ability of the *hexanuclears* to store a magnetic information is evaluated by its magnetic hysteresis measurements (Fig. 8). At 0.5 K, a broad opening of the magnetic hysteresis loop is observed (coercive field $H_c = 4100$ Oe, remnant magnetization $M_r = 19.83$ μ_B, 67% of the saturation value). The hysteresis is closed at 2 K (Fig. S18†). Within this range of temperature, the relaxation dynamics is ruled by the finite-size regime and the blocking temperature T_B in our operating conditions (magnetic field sweep rate of 15.5 Oe s^{-1}, with a τ_{exp} $= 21.3$ s) can be estimated considering the modified Arrhenius equation $T_B = \Delta_F/[k_B \ln(\tau_{exp}/\tau_F)] = 1.34 \pm 0.03$ K.

It is then clear from all magnetic measurements that the *hexanuclears*, despite being finite molecules, behave as SCM because they are molecules longer than the correlation length Δ_ξ they are hosting (Fig. 8). Interestingly, this difference between molecule length and correlation length is big enough to allow for the observation of finite and infinite relaxation regimes in the *hexanuclears*. This shows that spin-reversal can occur at an extremity of the molecule (finite regime) but as well on central position (infinite regime).

Hexanuclears show an enhanced SCM behavior when compared to *chains*. Indeed, they show a magnetic hysteresis that is steeper with H_c and M_R values almost doubled (Fig. 8). A dynamic magnetic relaxation with similar activation energies but slower relaxation times is also observed (Table 1). The reason for this optimized magnetic behavior could reside in the quality of the intra-molecular magnetic coupling between *chains* and *hexanuclears* because Tb^{III} magnetic anisotropies are almost similar between *chains* and *hexanuclears*. *Chains* are curled infinite molecules while *hexanuclears* form linear arrangements of finite molecules (Fig. 4). This second arrangement could favor efficient overlap of magnetic orbitals in the *hexanuclears*.

Conclusions

This study reports the investigation of what was a randomly appearing by-product of molecular chains and its rational synthesis into stable and pure batches of linear hexanuclear molecule. Its formation is triggered by moisture condition and the so-called *hexanuclear* shows an SCM behavior. Indeed, we demonstrate that a finite linear molecule can behave as an SCM if its length is big enough when compared to its magnetic correlation length. Additionally, by comparing the *hexanuclears* with their previously reported infinite counterparts, the *chains*, we show that the SCM behavior is enhanced in the former. This finding is important in the search for temperature- and air-stable

molecules for new molecular data storage devices. Indeed, SCMs host a robust magnetic relaxation that, contrary to the one observed on SMM, is not affected by under-barrier magnetic relaxation. Accordingly, the *hexanuclears* are promising candidates for surface deposition because they combine a good chemical stability with an SCM magnetic relaxation. This is a strong asset as molecules are far simpler to deposit on surfaces than chains that are insoluble by nature. Indeed, their deposition relies on their partial destruction to form finite objects with large and uncontrolled length distribution. On the contrary, the use of *hexanuclears* could be a way to form deposits of monodisperse SCM and enhance their ability to self-organize on surface.

Author contributions

Felix Houard: PhD in charge of the project. Frederic Gendron: Post-doc in charge of the theoretical calculations and quantum chemical simulations. Yan Suffren: As. Prof. in charge of the luminescence measurements. Thierry Guizouarn: Engineer in charge of very low temperature 3He magnetic measurments. Vincent Dorcet: Crystallographer. Guillaume Calvez: As. Prof. in charge of coupled ATG/IR investigation. Carole Daiguebonne: As. Prof. in charge of crystal structure refinements. Olivier Guillou: Prof. co-conceptor of the study. Boris Le Guennic: CNRS Research Director who coordinate the theoretical calculations and quantum chemical simulations. Matteo Mannini: As. Prof., co-director of F Houard PhD thesis, co-conceptor of the study. Kevin Bernot: As. Prof., co-director of F Houard PhD thesis, co-conceptor of the study, corresponding author.

Conflicts of interest

There are no conflicts to declare.

Acknowledgements

Notes and references

1 C. Coulon, H. Miyasaka and R. Clérac, in *Single-Molecule Magnets and Related Phenomena*, ed. R. Winpenny, Springer Berlin Heidelberg, 2006, pp. 163–206.

2 L. Bogani, A. Vindigni, R. Sessoli and D. Gatteschi, *J. Mater. Chem.*, 2008, **18**, 4750–4758.

3 A. Caneschi, D. Gatteschi, N. Lalioti, C. Sangregorio, R. Sessoli, G. Venturi, A. Vindigni, A. Rettori, M. G. Pini and M. A. Novak, *Angew. Chem., Int. Ed.*, 2001, **40**, 1760–1763.

4 G. Poneti, K. Bernot, L. Bogani, A. Caneschi, R. Sessoli, W. Wernsdorfer and D. Gatteschi, *Chem. Commun.*, 2007, 1807–1809.

5 H. Miyasaka, T. Madanbashi, K. Sugimoto, Y. Nakazawa, W. Wernsdorfer, K. Sugiura, M. Yamashita, C. Coulon and R. Clerac, *Chem.–Eur. J.*, 2006, **12**, 7029–7040.

6 V. Pianet, M. Urdampilleta, T. Colin, R. Clérac and C. Coulon, *Phys. Rev. B*, 2017, **96**, 214429.

7 J.-H. Wang, Z.-Y. Li, M. Yamashita and X.-H. Bu, *Coord. Chem. Rev.*, 2021, **428**, 213617.

8 J. Yang, Y.-F. Deng and Y.-Z. Zhang, *Dalton Trans.*, 2020, **49**, 4805–4810.

9 L. Shi, D. Shao, X.-Q. Wei, K. Dunbar and X. Wang, *Angew. Chem., Int. Ed.*, 2020, **59**, 10379–10384.

10 M. Rams, A. Jochim, M. Böhme, T. Lohmiller, M. Ceglarska, M. M. Rams, A. Schnegg, W. Plass and C. Näther, *Chem. - Eur. J.*, 2020, **26**, 2837.

11 F. Zhao, Z.-P. Dong, Z.-L. Liu and Y.-Q. Wang, *CrystEngComm*, 2019, **21**, 6958–6963.

12 C. Pichon, N. Suaud, C. Duhayon, N. Guihéry and J.-P. Sutter, *J. Am. Chem. Soc.*, 2018, **140**, 7698–7704.

13 C. Pichon, B. Elrez, V. Béreau, C. Duhayon and J. P. Sutter, *Eur. J. Inorg. Chem.*, 2018, **2018**, 340–348.

14 W. Jiang, C. Jiao, Y. Meng, L. Zhao, Q. Liu and T. Liu, *Chem. Sci.*, 2018, **9**, 617–622.

15 Q. Liu, J.-X. Hu, Y.-S. Meng, W.-J. Jiang, J.-L. Wang, W. Wen, Q. Wu, H.-L. Zhu, L. Zhao and T. Liu, *Angew. Chem., Int. Ed.*, 2021, **60**, 10537.

16 M. G. F. Vaz, R. A. A. Cassaro, H. Akpinar, J. A. Schlueter, P. M. Lahti and M. A. Novak, *Chem. - Eur. J.*, 2014, **20**, 5460–5467.

17 E. Bartolome, J. Bartolome, S. Melnic, D. Prodius, S. Shova, A. Arauzo, J. Luzon, L. Badia-Romano, F. Luis and C. Turta, *Dalton Trans.*, 2014, **43**, 10999–11013.

18 X. Zhang, S. Liu, V. Vieru, N. Xu, C. Gao, B. W. Wang, W. Shi, L. F. Chibotaru, S. Gao, P. Cheng and A. K. Powell, *Chem. - Eur. J.*, 2018, **24**, 6079–6086.

19 J. Jung, F. Le Natur, O. Cador, F. Pointillart, G. Calvez, C. Daiguebonne, O. Guillou, T. Guizouarn, B. Le Guennic and K. Bernot, *Chem. Commun.*, 2014, **50**, 13346–13348.

20 W.-B. Chen, L. Zhong, Y.-J. Zhong, Y.-Q. Zhang, S. Gao and W. Dong, *Inorg. Chem. Front.*, 2020, **7**, 3136–3145.

21 M. Al Hareri, Z. Ras Ali, J. Regier, E. L. Gavey, L. D. Carlos, R. A. S. Ferreira and M. Pilkington, *Inorg. Chem.*, 2017, **56**(13), 7344–7353.

22 E. Bartolome, J. Bartolome, A. Arauzo, J. Luzon, L. Badia, R. Cases, F. Luis, S. Melnic, D. Prodius, S. Shova and C. Turta, *J. Mater. Chem. C*, 2016, **4**, 5038–5050.

23 R. Ababei, C. Pichon, O. Roubeau, Y.-G. Li, N. Bréfuel, L. Buisson, P. Guionneau, C. Mathonière and R. Clérac, *J. Am. Chem. Soc.*, 2013, **135**, 14840–14853.

24 G. Huang, G. Fernandez-Garcia, I. Badiane, M. Camara, S. Freslon, O. Guillou, C. Daiguebonne, F. Totti, O. Cador,

T. Guizouarn, B. Le Guennic and K. Bernot, *Chem. - Eur. J.*, 2018, **24**, 6983–6991.

25 G. Huang, X. Yi, F. Gendron, B. Le Guennic, T. Guizouarn, C. Daiguebonne, G. Calvez, Y. Suffren, O. Guillou and K. Bernot, *Dalton Trans.*, 2019, **48**, 16053–16061.

26 T. Liu, H. Zheng, S. Kang, Y. Shiota, S. Hayami, M. Mito, O. Sato, K. Yoshizawa, S. Kanegawa and C. Duan, *Nat. Commun.*, 2013, **4**, 2826.

27 N. Hoshino, F. Iijima, G. N. Newton, N. Yoshida, T. Shiga, H. Nojiri, A. Nakao, R. Kumai, Y. Murakami and H. Oshio, *Nat. Chem.*, 2012, **4**, 921–926.

28 D.-P. Dong, T. Liu, S. Kanegawa, S. Kang, O. Sato, C. He and C.-Y. Duan, *Angew. Chem., Int. Ed.*, 2012, **51**, 5119–5123.

29 M. Hojorat, H. Al Sabea, L. Norel, K. Bernot, T. Roisnel, F. Gendron, B. Le Guennic, E. Trzop, E. Collet, J. R. Long and S. Rigaut, *J. Am. Chem. Soc.*, 2020, **142**, 931–936.

30 M. Scarrozza, P. Barone, R. Sessoli and S. Picozzi, *J. Mater. Chem. C*, 2016, **4**, 4176–4185.

31 M. Fittipaldi, A. Cini, G. Annino, A. Vindigni, A. Caneschi and R. Sessoli, *Nat. Mater.*, 2019, **18**, 239–334.

32 M. Atzori, F. Santanni, I. Breslavetz, K. Paillot, A. Caneschi, G. L. J. A. Rikken, R. Sessoli and C. Train, *J. Am. Chem. Soc.*, 2020, **142**, 13908–13916.

33 I. Mihalcea, M. Perfetti, F. Pineider, L. Tesi, V. Mereacre, F. Wilhelm, A. Rogalev, C. E. Anson, A. K. Powell and R. Sessoli, *Inorg. Chem.*, 2016, **55**, 10068–10074.

34 O. Roubeau, A. Colin, V. Schmitt and R. Clérac, *Angew. Chem., Int. Ed.*, 2004, **43**, 3283–3286.

35 P. Grondin, O. Roubeau, M. Castro, H. Saadaoui, A. Colin and R. CléRac, *Langmuir*, 2010, **26**, 5184–5195.

36 X. Meng, W. Shi and P. Cheng, *Coord. Chem. Rev.*, 2019, **378**, 134–150.

37 D. Luneau, *Eur. J. Inorg. Chem.*, 2020, **2020**, 597–604.

38 J. Sun, J. Xie, L. Li and J.-P. Sutter, *Inorg. Chem. Front.*, 2020, **7**, 1949–1956.

39 J. Xie, H.-D. Li, M. Yang, J. Sun, L.-C. Li and J.-P. Sutter, *Chem. Commun.*, 2019, **55**, 3398–3401.

40 W. Shi, X. Liu, X. Feng, K. R. Meihaus, X. Meng, Y. Zhang, L. Li, J.-L. Liu, Y.-Q. Zhang, P. Cheng and J. R. Long, *Angew. Chem., Int. Ed.*, 2020, **59**, 10610–10618.

41 X. Liu, Y.-X. Wang, Z. Han, T. Han, W. Shi and P. Cheng, *Dalton Trans.*, 2019, **48**, 8989–8994.

42 X. Liu, Y. Zhang, W. Shi and P. Cheng, *Inorg. Chem.*, 2018, **57**, 13409–13414.

43 R. A. A. Cassaro, S. G. Reis, T. S. Araujo, P. M. Lahti, M. A. Novak and M. G. F. Vaz, *Inorg. Chem.*, 2015, **54**, 9381–9383.

44 M. G. F. Vaz and M. Andruh, *Coord. Chem. Rev.*, 2021, **427**, 213611.

45 D. Luneau and P. Rey, *Coord. Chem. Rev.*, 2005, **249**, 2591–2611.

46 C. Benelli and D. Gatteschi, *Chem. Rev.*, 2002, **102**, 2369–2388.

47 K. Katoh, K. Kagesawa and M. Yamashita, in *World Scientific Reference on Spin in Organics*, 2018, pp. 271–344.

48 S. Demir, I.-R. Jeon, J. R. Long and T. D. Harris, *Coord. Chem. Rev.*, 2015, **289–290**, 149–176.

49 F. Houard, Q. Evrard, G. Calvez, Y. Suffren, C. Daiguebonne, O. Guillou, F. Gendron, B. Le Guennic, T. Guizouarn, V. Dorcet, M. Mannini and K. Bernot, *Angew. Chem., Int. Ed.*, 2020, **59**, 780–784.

50 C. Janiak, *J. Chem. Soc., Dalton Trans.*, 2000, 3885–3896.

51 I. Y. Bagryanskaya, L. V. Politanskaya and E. V. Tretyakov, *Inorg. Chem. Commun.*, 2016, **66**, 47–50.

52 Q. Evrard, G. Cucinotta, F. Houard, G. Calvez, Y. Suffren, C. Daiguebonne, O. Guillou, A. Caneschi, M. Mannini and K. Bernot, *Beilstein J. Nanotechnol.*, 2019, **10**, 2440–2448.

53 G. A. Timco, T. B. Faust, F. Tuna and R. E. P. Winpenny, *Chem. Soc. Rev.*, 2011, **40**, 3067–3075.

54 G. F. S. Whitehead, F. Moro, G. A. Timco, W. Wernsdorfer, S. J. Teat and R. E. P. Winpenny, *Angew. Chem., Int. Ed.*, 2013, **52**, 9932–9935.

55 B. Koen, J. C. B. K. A. Gschneidner and V. K. Pecharsky, in *Handbook on the Physics and Chemistry of Rare Earths*, Elsevier, 2005, pp. 107–272.

56 R. Beaulac, G. Bussiere, C. Reber, C. Lescop and D. Luneau, *New J. Chem.*, 2003, **27**, 1200–1206.

57 A. Lannes, M. Intissar, Y. Suffren, C. Reber and D. Luneau, *Inorg. Chem.*, 2014, **53**, 9548–9560.

58 C. Lescop, G. Bussiere, R. Beaulac, H. Belisle, E. Belorizky, P. Rey, C. Reber and D. Luneau, *J. Phys. Chem. Solids*, 2004, **65**, 773–779.

59 G. Cucinotta, M. Perfetti, J. Luzon, M. Etienne, P.-E. Car, A. Caneschi, G. Calvez, K. Bernot and R. Sessoli, *Angew. Chem., Int. Ed.*, 2012, **51**, 1606–1610.

60 M. Böhme and W. Plass, *Chem. Sci.*, 2019, **10**, 9189–9202.

61 J. Jung, M. Puget, O. Cador, K. Bernot, C. J. Calzado and B. Le Guennic, *Inorg. Chem.*, 2017, **56**, 6788–6801.

62 M. Ferbinteanu, H. Miyasaka, W. Wernsdorfer, K. Nakata, K.-i. Sugiura, M. Yamashita, C. Coulon and R. Clérac, *J. Am. Chem. Soc.*, 2005, **127**, 3090–3099.

63 M. Ding, B. Wang, Z. Wang, J. Zhang, O. Fuhr, D. Fenske and S. Gao, *Chem. - Eur. J.*, 2012, **18**, 915–924.

64 C. Coulon, R. Clérac, W. Wernsdorfer, T. Colin, A. Saitoh, N. Motokawa and H. Miyasaka, *Phys. Rev. B*, 2007, **76**, 214422.

65 M. G. Pini, A. Rettori, L. Bogani, A. Lascialfari, M. Mariani, A. Caneschi and R. Sessoli, *Phys. Rev. B*, 2011, **84**, 094444.

66 C. V. Topping and S. J. Blundell, *J. Phys.: Condens. Matter*, 2018, **31**, 013001.

67 K. S. Cole and R. H. Cole, *J. Chem. Phys.*, 1941, **9**, 341–351.

68 C. Dekker, A. F. M. Arts, H. W. de Wijn, A. J. van Duyneveldt and J. A. Mydosh, *Phys. Rev. B*, 1989, **40**, 11243–11251.

69 R. J. Glauber, *J. Math. Phys.*, 1963, **4**, 294–307.

70 L. Bogani, R. Sessoli, M. G. Pini, A. Rettori, M. A. Novak, P. Rosa, M. Massi, M. E. Fedi, L. Giuntini, A. Caneschi and D. Gatteschi, *Phys. Rev. B*, 2005, 72.

71 J. H. Luscombe, M. Luban and J. P. Reynolds, *Phys. Rev. E: Stat. Phys., Plasmas, Fluids, Relat. Interdisc. Top.*, 1996, **53**, 5852–5860.